NSRRC - J0U314 (2014)

THE JOURNAL OF PHYSICAL CHEMISTRY C

Article

pubs.acs.org/JPCC

Reassembly and Oxidation of a Silver Nanoparticle Bilayer Probed by in Situ X-ray Reciprocal Space Mapping

Peter Siffalovic,*[,†] Karol Vegso,[†] Monika Benkovicova,[†] Matej Jergel,[†] Andrej Vojtko,[†] Martin Hodas,[†] Stefan Luby,[†] Hsin-Yi Lee,[‡] Ching-Shun Ku,[‡] Man-Ling Lin,[‡] U-Ser Jeng,[‡] Chun-Jen Su,[‡] and Eva Majkova[†]

[†]Institute of Physics, SAS, Dubravska cesta 9, 845 11 Bratislava, Slovakia

[‡]National Synchrotron Radiation Research Center, 101 Hsin-Ann Road, Hsinchu 30076, Taiwan

ABSTRACT: We report on an in situ observation of reassembly and oxidation of a self-assembled silver nanoparticle bilayer due to an UV/ozone treatment and removal of the nanoparticle surfactant molecules. Such arrays of metal oxide nanoparticles are designated for sensor applications. To follow simultaneously the temporal evolution of particular processes taking place at different length scales, we employed the small- and wide-angle X-ray scattering in situ. In this way, all relevant transformation stages were identified: removal of the nanoparticle surfactant shell accompanied by a loss of the nanoparticle position correlations, oxidation of the nanoparticle crystalline core, and final reassembly of the silver oxide nanoparticles into agglomerates. Study of these processes on a common timeline provides a detailed insight into the kinetics of the UV/ozone treatment which represents a simple and effective method for preparation of metal oxide nanoparticle arrays for sensors.

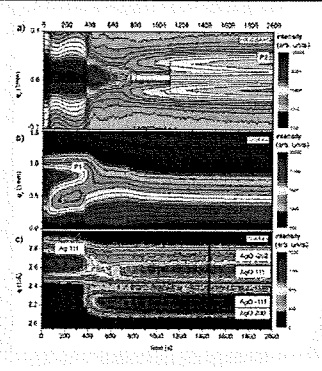

INTRODUCTION

Self-assembled metallic and metal oxide nanoparticle layers are in the focus of contemporary sensor applications. The latest generation of strain gauges is based on multilayers of metallic nanoparticles to name only a few of them.[1−3] Measured electrical resistivity as a function of the applied mechanical stress is extremely sensitive to the nanoparticle spacing due to the tunneling regime of electrical conductivity that outperforms conventional metal film based strain gauges.[4] Another essential nanoparticle application is found in semiconducting metal oxide gas sensors.[5,6] The sensing properties of metal oxide gas sensors are related to the surface reactions with the detected gases. Therefore the multilayers of self-assembled semiconducting metal oxide nanoparticles represent an ideal platform for gas sensing due to a significantly enhanced surface/volume ratio available for these surface reactions.[7−10] Our recent studies have revealed a parts per billion (ppb) sensitivity of self-assembled iron oxide and cobalt iron oxide nanoparticle arrays to NO_2 gases released by common explosives.[11,12] Self-assembled nanoparticle layers are also attractive as templates for the surface-enhanced Raman scattering studies.[13−15] All the presented applications demonstrate a growing interest in the self-assembled nanoparticle arrays in the advanced sensor technologies.

In this paper, we present a detailed study of the surfactant removal and oxidation of a self-assembled bilayer of silver nanoparticles that represents the simplest self-assembled structure used in advanced nanoparticle-based gas sensors.[8] The gas-sensing function is based on exposure of the nanoparticle metal oxide surface to residual gases in ambient atmosphere to initiate chemical reactions. For this purpose, the nanoparticle organic shell (surfactant) has to be removed e.g. in a UV/ozone reactor, which is a common approach. Here, the UV photolysis and ozonolysis are the key processes to remove the organic molecules attached to the nanoparticle surface.[16,17] The UV/ozone treatment of a self-assembled nanoparticle monolayer results in a discontinuous layer with many defects and voids.[18] Such a submonolayer is not suitable for gas-sensing applications. On the other hand, the UV/ozone treatment of a nanoparticle bilayer results in a continuous nanoparticle film. The conventional real-space imaging techniques like scanning electron microscopy (SEM) or atomic force microscopy (AFM) are unable to follow the nanoparticle removal in the UV/ozone reactor in real time. Therefore we employed the reciprocal space mapping (RSM) of the nanoparticle reassembly and oxidation by the small- and wide-angle X-ray scattering, respectively, performed simultaneously with high brilliance synchrotron radiation. These synchrotron-based techniques can easily track in situ the reciprocal space of nanoparticle arrays from reciprocal angstroms to reciprocal micrometers.[19−21] In the result, we can observe a nanoparticle self- and/or reassembly from nanometers up to micrometers and simultaneously phase transitions at the atomic level inside the nanoparticles with temporal resolution down to milliseconds.

Received: December 30, 2013
Revised: March 10, 2014
Published: March 12, 2014

 © 2014 American Chemical Society

EXPERIMENTAL METHODS

The self-assembled nanoparticle bilayer was deposited by a modified Langmuir–Schaefer deposition.[22] Chemical synthesis of the silver nanoparticles was published elsewhere.[23] The radially averaged small-angle X-ray scattering (SAXS) curve from the nanoparticles dispersed in chloroform is shown in Figure 1. The experimental data were fitted with a model based

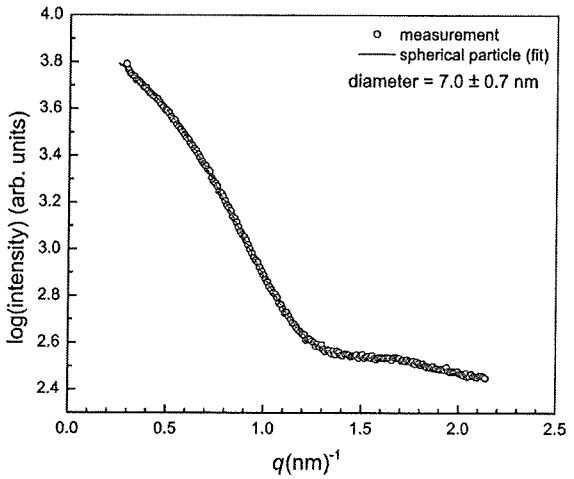

Figure 1. SAXS: experimental data and fit of silver nanoparticles in colloidal solution.

on spherical particles with the Gaussian distribution of particle diameter. The nanoparticle mean core size and its standard deviation were determined to be 7 and 0.7 nm, respectively. The nanoparticle surfactant shell is composed of oleic acid and oleylamine molecules. The as prepared silver nanoparticles were dispersed in chloroform (99.8%, HPLC grade) at a concentration of 0.2 mg/mL. The nanoparticle dispersion was applied on the water surface (specific electrical resistance >18 MΩ·cm) with use of a microsyringe. After evaporation of the solvent, a nanoparticle monolayer[24] was formed at a surface pressure of 21 mN/m, being subsequently transferred onto a Si substrate terminated by a 300 nm thick Si_3N_4 layer. Repeating the above-described deposition process, we fabricated a vertically uncorrelated nanoparticle bilayer. The time-resolved in situ grazing-incidence small-angle (GISAXS) and wide-angle (GIWAXS) X-ray scattering experiments were performed at the BL23A endstation of the National Synchrotron Radiation Research Center (NSRRC), Taiwan. The detailed description of the BL23A beamline can be found elsewhere.[25] The X-ray beam incident angle was fixed at 0.4° and the X-ray energy was set to 15 keV. The single frame exposure time was set to 5 s. The simultaneous GISAXS and GIWAXS reciprocal space maps were recorded by synchronized MAR165 CCD (165 mm diameter) and CMOS flat planel X-ray detector C9728DK (52.8 mm square), respectively. The scattering wavevectors were calibrated with use of silver behenate. The sample was located in a custom designed window-less UV reactor equipped with an ozone-generating low-pressure mercury lamp ($h\nu$ = 4.9, 6.7 eV). The total UV intensity at the sample surface was estimated to be 2 mW/cm^2. The UV/ozone reactor was started 30 s after activation of the simultaneous GISAXS/GIWAXS measurements. The sample surface morphology was measured in tapping mode ex situ, using Bruker Dimension AFM (cantilever TESPA, Bruker).

RESULTS AND DISCUSSION

The Figure 2a shows the GISAXS reciprocal space pattern taken 30 s after starting the measurement and before switching

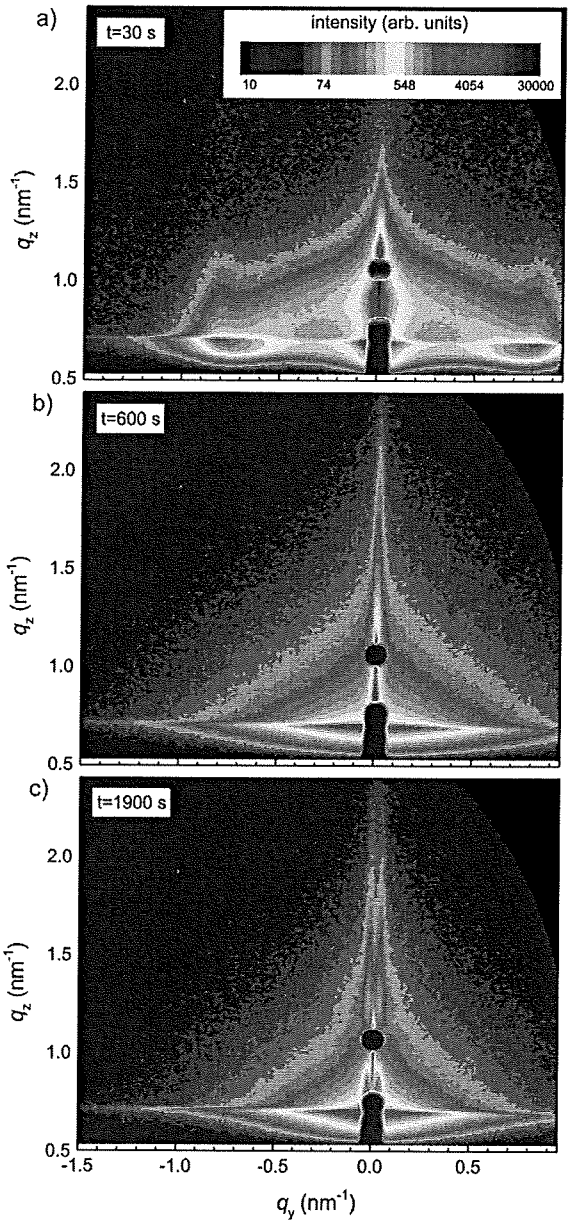

Figure 2. GISAXS reciprocal space maps of the UV/ozone treated nanoparticle bilayer at t = 30 (a), 600 (b), and 1900 s (c) after starting the measurements.

on the UV/ozone reactor. The most prominent features visible in the pristine GISAXS reciprocal space map are the two symmetrical diffraction Bragg rods ±10 located at $q_y^{max} = \pm 0.77$ nm^{-1}. These two Bragg rods correspond to the in-plane correlations of nanoparticle positions in the self-assembled bilayer.[24] The intensity modulation of Bragg rods along q_y

dx.doi.org/10.1021/jp4127573 | J. Phys. Chem. C 2014, 118, 7195–7201

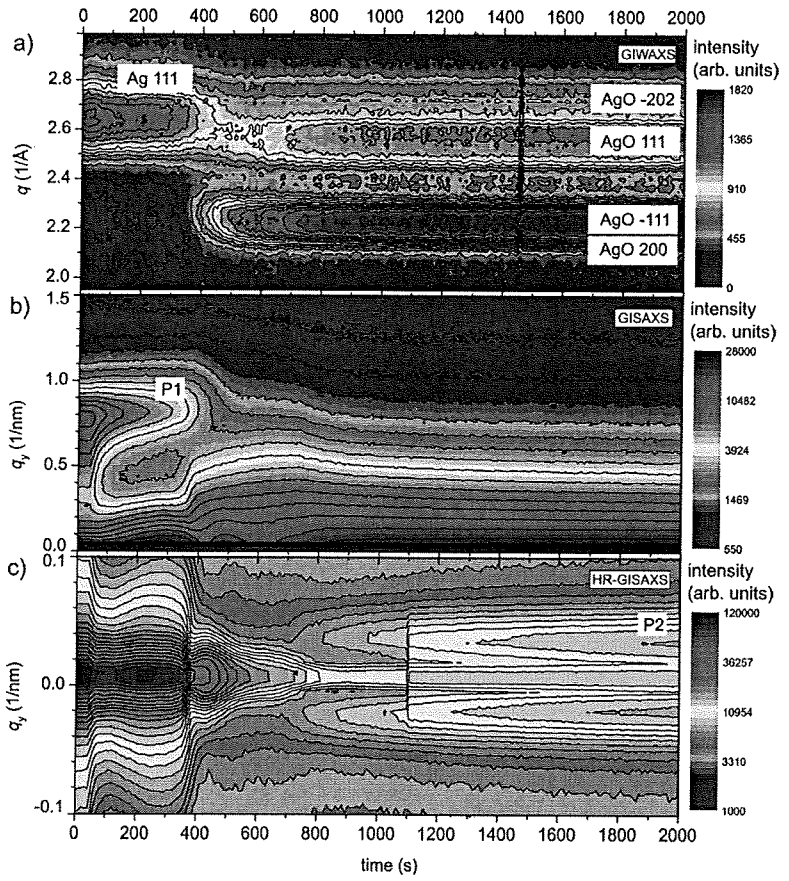

Figure 3. Temporal evolution of the selected cuts along q_y in the reciprocal space: (a) GIWAXS, (b) GISAXS, and (c) HR-GISAXS. For a closer explanation see the text.

direction is given by minima in the nanoparticle form factor function.[26] Assuming hexagonally ordered close-packed spherical nanoparticles, the hexagonal lattice spacing d_{10} is related to the Bragg maximum position[27] q_y^{max} as $d_{10} = 2\pi/q_y^{max}$. Accordingly, the nearest-neighbor nanoparticle distance[28] Δ equals 9.4 nm ($\Delta = 2d_{10}/\sqrt{3}$). Considering the core nanoparticle diameter of 7 ± 0.7 nm measured by SAXS in solution, the thickness of the surfactant shell[27] is approximately 1.2 nm. This surfactant shell was gradually removed by photolysis and ozonolysis when the UV/ozone reactor was switched on 30 s after starting the GISAXS/GIWAXS measurements. Figure 2b shows an intermediate state after 600 s. The Bragg rods visible at the early surfactant removal times disappeared completely and the reciprocal space map shows no signs of the in-plane nanoparticle position correlations. Figure 2c shows the final GISAXS reciprocal space map after 1900 s where new Bragg rods at $q_y^{max} = \pm 0.026$ nm^{-1} are visible. These Bragg rods correspond to the mean lateral correlation length $\xi \cong 240$ nm ($\xi = 2\pi/q_y^{max}$) of the oxidized nanoparticle agglomerates.

To quantify the temporal evolution of the loss of the original nanoparticle self-assembly and the final nanoparticle agglomeration as well as the phase transition due to oxidation of the silver nanoparticles, we integrated specific areas in the reciprocal space and plotted them as a function of the UV/ozone treatment time. Figure 3a shows the temporal evolution of GIWAXS obtained by a pie-integration for q values between 1.9 and 3.0 Å^{-1}. For the pristine silver nanoparticle layers, the Ag 111 diffraction is observable.[29] In the oxidized state, we can identify the following AgO diffraction lines:[29] −202, 111, −111, 200. Figure 4a shows the integrated area under the Ag 111 and AgO −111 diffractions. The fwhm of the AgO −111 diffraction peak is plotted in Figure 4b along with the evaluated AgO unit cell volume. Figure 3b depicts the temporal evolution of the line cuts along q_y integrated between q_z values of 0.675 and 0.725 nm^{-1}. In the following we will refer to this plot as the time-resolved GISAXS. Here, the P1 symbol is assigned to one of the Bragg rods stemming from the pristine nanoparticle position correlations in the self-assembled bilayer. The integrated area under the P1 peak is shown in Figure 4c and the maximum position and fwhm of the P1 peak are plotted in Figure 4d. Finally, Figure 3c shows the temporal evolution of the line cuts along q_y integrated between q_z values of 0.8 and 0.85 nm^{-1}. We will refer to this plot as the time-resolved high-resolution GISAXS (HR-GISAXS). The most prominent features are new Bragg rods, one of them being denoted as P2. The temporal evolution of the integrated area under the P2 peak is shown in Figure 4c while the fitted P2 peak maximum position and full width at half-maximum (fwhm) are plotted in Figure 4d.

To analyze further the nanoparticle reassembly during the surfactant removal, we performed numerical simulations of the GISAXS reciprocal space map based on the azimuthally averaged two-dimensional (2D) paracrystal model of the self-

dx.doi.org/10.1021/jp4127573 | J. Phys. Chem. C 2014, 118, 7195−7201

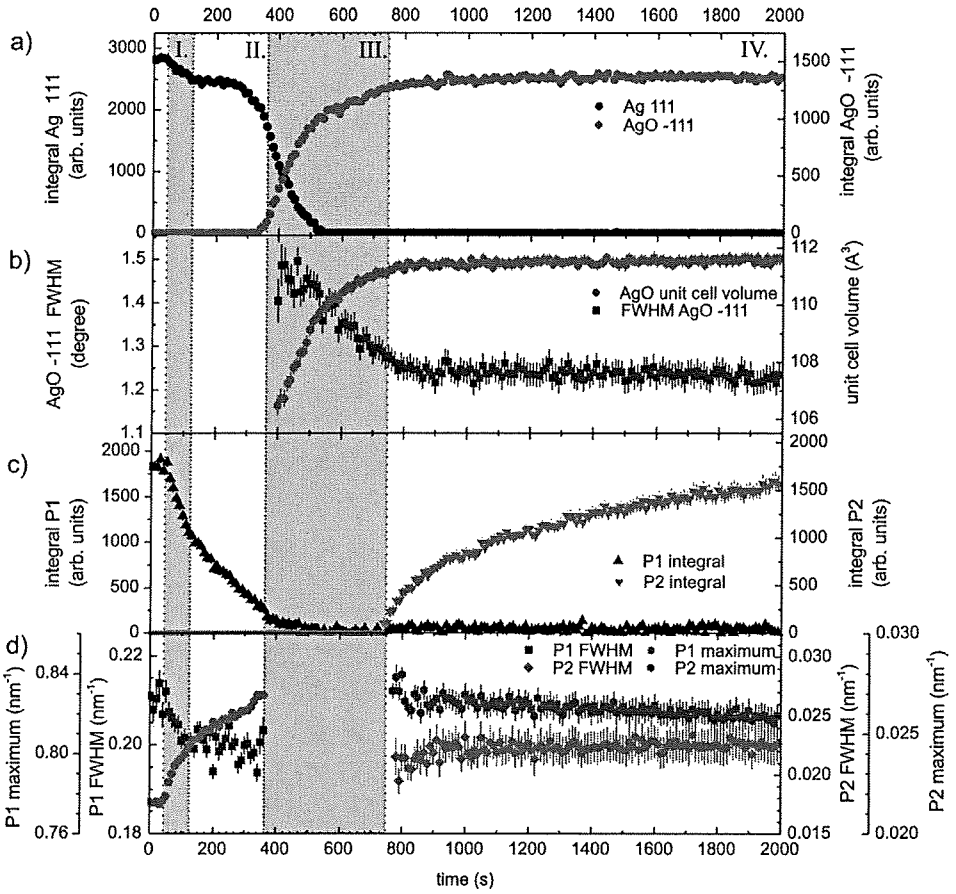

Figure 4. Time dependence of some selected parameters extracted from the reciprocal space cuts shown in Figure 3. The distinct treatment stages are marked by Roman numbers and discussed in the text.

assembled nanoparticle layers in the Local Monodisperse Approximation (LMA) within the framework of the distorted-wave Born approximation (DWBA).[30] In particular, analysis of the reciprocal space cuts along the q_y direction at the critical exit angle of a vertically uncorrelated nanoparticle bilayer can be reduced to a simulation of the nanoparticle monolayer as reported previously.[26] Following this strategy, we calculated equipotential lines for the maximum positions and fwhm values around the values of the P1 Bragg peak in the landscape of the nanoparticle distance Δ and the degree of paracrystal disorder g in the 2D paracrystal (Figure 5). Hence, the values of these paracrystal parameters can be read out for any time of the UV/ozone treatment when plotting a couple of the corresponding experimental P1 peak values into this landscape.

Relying on the measured temporal evolution of the reciprocal space as shown in Figures 3 and 4 and applying the paracrystal model as presented in Figure 5, we can introduce a nanoparticle UV/ozone treatment scenario that can be divided into four stages as indicated in Figure 4 by Roman numbers. In the first stage I, instantly after switching on the UV/ozone reactor, we observe a gradual decrease of the integrated area under the P1 Bragg peak which implies a loss of the correlations in the self-assembled nanoparticle array due to the gradual removal of the surfactant molecules (Figure 4c). Two noteworthy effects accompany this correlation decay. First, a gradual shift of the P1 Bragg peak toward higher q_y values suggests a mean

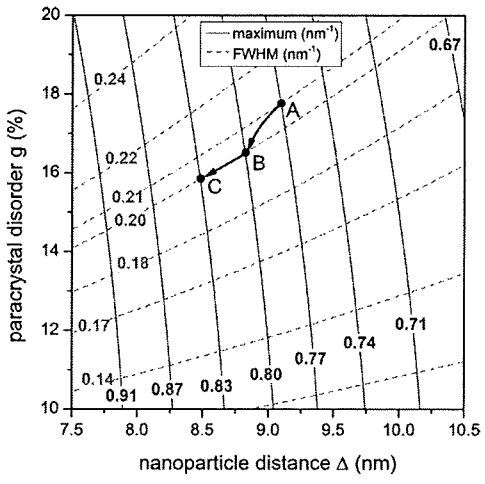

Figure 5. Brag rod width and maximum position equipotential lines calculated for different paracrystal configurations characterized by the nanoparticle distance Δ and paracrystal disorder g. The letters A, B, and C refer to the experimental values read out from the P1 peak (see Figure 3) at the beginning of stage I, end of stage I, and end of stage II, respectively, showing experimental trajectory in the landscape of the paracrystal model.

dx.doi.org/10.1021/jp4127573 | J. Phys. Chem. C 2014, 118, 7195−7201

interparticle spacing reduction and a nanoparticle array densification (Figure 4d) that can be attributed to better filing up the voids in the bottom layer by the nanoparticles from the top one during the rearrangement. Second, the narrowing fwhm of the P1 Bragg peak implies a locally enhanced nanoparticle correlation in the bottom layer (Figure 4d). Hence, though the overall number of the laterally correlated nanoparticles decreases, the original short-range order in the rest of the self-assembled regions is temporarily improved before their extinction. This can be confirmed also within the concept of the paracrystal model. In particular, the P1 Bragg peak maximum position and width (fwhm) at the beginning of stage I plotted in the paracrystal landscape and labeled by letter A (Figure 5) show the initial nanoparticle distance Δ of 9.1 nm and the paracrystal disorder g of 17.8% which decrease to 8.8 nm and 16.5%, respectively, during the surfactant removal at the end of stage I (marked by letter B). This evolution persists also in stage II, which is characterized by further decay of the nanoparticle correlations (as evidenced by the decreasing integrated area under the P1 Bragg peak) and further reduction of the mean interparticle distance (as shown by the P1 Bragg peak shift toward higher q_y values) (Figure 4c,d). Although the P1 Bragg peak width stays constant in stage II, the paracrystal disorder g further decreases as visualized by the transition from point B to C along the equipotential line at the end of stage II (Figure 5). In particular, the interparticle distance Δ and the paracrystal disorder g are lowered to 8.5 nm and 15.8%, respectively.

In the GIWAXS, a decrease of the integrated area under the Ag 111 diffraction is observed to the end of stage II and continues in stage III where the appearance of the AgO monoclinic phase due to the nanoparticle surface oxidation after the surfactant removal is detected and tracked by a strong −111 diffraction (Figure 4a). The oxidation is completed to the end of stage III. Due to the grazing-incidence geometry, the AgO −111 diffraction is strongly convoluted with the irradiated sample area, which hampers a quantitative estimate of the AgO crystalline phase portion in the nanoparticle volume. Nevertheless, evaluating the temporal evolution of different AgO diffractions, we can evaluate a change of the AgO unit cell volume. In particular, it gradually increases from 107 Å^3 at the initial stages of the AgO formation, which is the nominal value of the unstrained monoclinic AgO phase,[29] and saturates at the end of stage III (Figure 4b). The growth of the AgO phase in the nanoparticle volume is accompanied also by a fwhm decrease of AgO −111 diffraction, which suggests a more regular space lattice.

The GISAXS and/or HR-GISAXS reciprocal space maps do not exhibit any Bragg rods in stage III (Figure 3b,c), suggesting the absence of any nanoparticle correlations. Contrarily, new Bragg rods appear at $q_y = \pm 0.026$ nm^{-1} corresponding to a typical correlation length of approximately 240 nm in real space in stage IV (P2 in Figure 3c). This indicates a self-assembly of AgO nanoparticles in the form of large nanoparticle domains which continues obviously even after 2000 s as the P2 peak integral intensity does not come to saturation here. To better understand the agglomeration stage IV, we performed ex situ AFM measurements in the pristine and agglomeration stages as shown in Figure 6, parts a and b, respectively. The calculated radially averaged power spectra densities (PSD) of surface morphology for the pristine and agglomerated nanoparticle states are shown in Figure 6c. The q_y position of the P2 Bragg peak from HR-GISAXS can be directly compared to the PSD

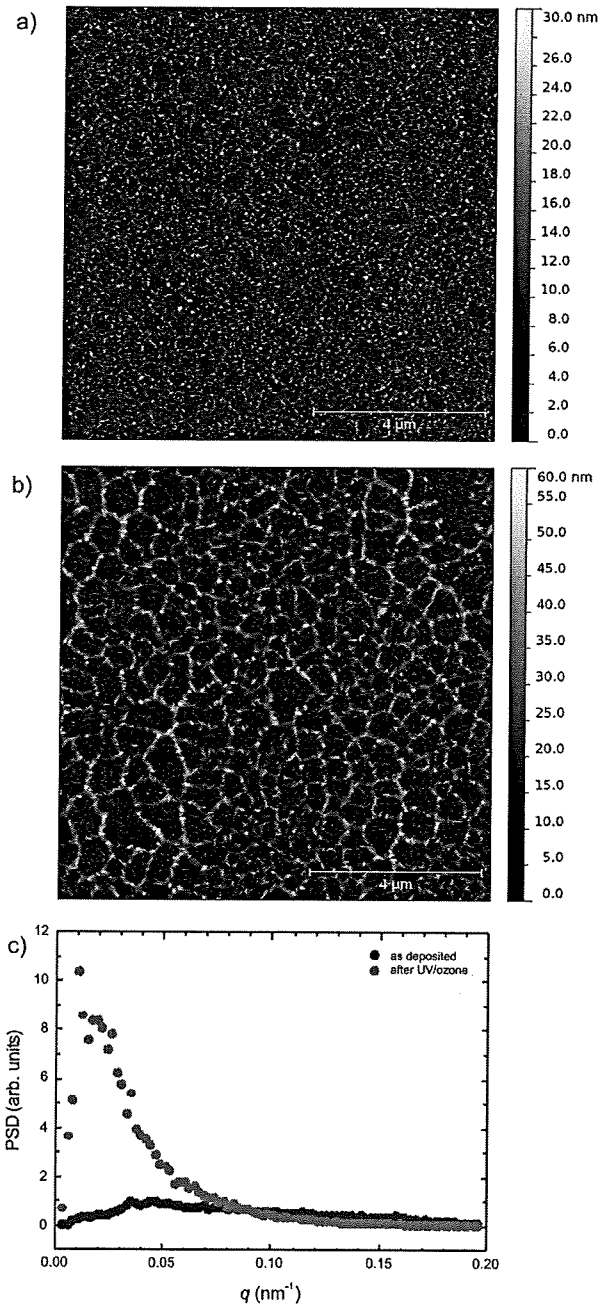

Figure 6. The AFM topography images of the self-assembled nanoparticle bilayer (a) before and (b) after the UV/ozone treatment and (c) the corresponding radially averaged power spectral density function.

data obtained from AFM, showing a rather good agreement at 0.02 nm^{-1}. Hence, formation of a percolated network of AgO nanoparticles in stage IV can be concluded. The fwhm of P2 peak is constant during the nanoparticle agglomeration phase (Figure 4d), which indicates a stable lateral correlation length during the agglomeration process.

dx.doi.org/10.1021/jp4127573 | J. Phys. Chem. C 2014, 118, 7195−7201

CONCLUSIONS

Details of the silver nanoparticle bilayer reassembly and oxidation kinetics on the UV/ozone treatment were studied by simultaneous application of the GISAXS and GIWAXS techniques which allow a precise nanoparticle tracking under harsh treatment conditions, not accessible by other analytical techniques. Four distinct stages of the system response to the UV/ozone treatment were identified. The first two stages involve a gradual surfactant removal accompanied by the decay of the nanoparticle self-assembly. The third stage is governed by the oxidation of bare silver nanoparticles which exhibit no position correlations. The fourth stage is characterized by the onset and proceeding agglomeration of the oxidized nanoparticles which is not stopped even after 2000 s. This detailed knowledge of the nanoparticle UV/ozone treatment has direct implications for preparation of advanced sensors based on metal oxide nanoparticles.

AUTHOR INFORMATION

Corresponding Author

*E-mail: peter.siffalovic@savba.sk. Tel: +421-2-20910766.

Notes

The authors declare no competing financial interest.

ACKNOWLEDGMENTS

The work was supported by the Grant Agency VEGA Bratislava, project no. 2/0041/11, and Centre of Excellence SAS FUN-MAT. The support of the SAS-NSC JRP 2011/05, SAS-TUBITAK JRP 2013/6, Slovak Research and Development Agency, project No. APVV-0308-11 and XOPTICS projects as well as COST Action CM1101 is also acknowledged.

REFERENCES

(1) Farcau, C.; Moreira, H.; Viallet, B.; Grisolia, J.; Ciuculescu-Pradines, D.; Amiens, C.; Ressier, L. Monolayered Wires of Gold Colloidal Nanoparticles for High-Sensitivity Strain Sensing. *J. Phys. Chem. C* **2011**, *115*, 14494–14499.

(2) Farcau, C.; Sangeetha, N. M.; Moreira, H.; Viallet, B.; Grisolia, J.; Ciuculescu-Pradines, D.; Ressier, L. High-Sensitivity Strain Gauge Based on a Single Wire of Gold Nanoparticles Fabricated by Stop-and-Go Convective Self-Assembly. *ACS Nano* **2011**, *5*, 7137–7143.

(3) Herrmann, J.; Müller, K.-H.; Reda, T.; Baxter, G. R.; Raguse, B.; de Groot, G. J. J. B.; Chai, R.; Roberts, M.; Wieczorek, L. Nanoparticle Films as Sensitive Strain Gauges. *Appl. Phys. Lett.* **2007**, *91*, 183105.

(4) Moreira, H.; Grisolia, J.; Sangeetha, N. M.; Decorde, N.; Farcau, C.; Viallet, B.; Chen, K.; Viau, G.; Ressier, L. Electron Transport in Gold Colloidal Nanoparticle-Based Strain Gauges. *Nanotechnology* **2013**, *24*, 095701.

(5) Wang, C.; Yin, L.; Zhang, L.; Xiang, D.; Gao, R. Metal Oxide Gas Sensors: Sensitivity and Influencing Factors. *Sensors* **2010**, *10*, 2088–2106.

(6) Franke, M. E.; Koplin, T. J.; Simon, U. Metal and Metal Oxide Nanoparticles in Chemiresistors: Does the Nanoscale Matter? *Small* **2006**, *2*, 36–50.

(7) Leite, E. R.; Weber, I. T.; Longo, E.; Varela, J. A. A New Method to Control Particle Size and Particle Size Distribution of SnO_2 Nanoparticles for Gas Sensor Applications. *Adv. Mater.* **2000**, *12*, 965–968.

(8) Luby, S.; Chitu, L.; Jergel, M.; Majkova, E.; Siffalovic, P.; Caricato, A. P.; Luches, A.; Martino, M.; Rella, R.; Manera, M. G. Oxide Nanoparticle Arrays for Sensors of CO and NO_2 Gases. *Vacuum* **2012**, *86*, 590–593.

(9) Nayral, C.; Ould-Ely, T.; Maisonnat, A.; Chaudret, B.; Fau, P.; Lescouzères, L.; Peyre-Lavigne, A. A Novel Mechanism for the Synthesis of Tin/Tin Oxide Nanoparticles of Low Size Dispersion and of Nanostructured SnO_2 for the Sensitive Layers of Gas Sensors. *Adv. Mater.* **1999**, *11*, 61–63.

(10) Wang, J.-J.; Lv, A.-F.; Wang, Y.-Q.; Cui, B.; Yan, H.-J.; Hu, J.-S.; Hu, W.-P.; Guo, Y.-G.; Wan, L.-J. Integrated Prototype Nanodevices via SnO_2 Nanoparticles Decorated SnSe Nanosheets. *Sci. Rep.* **2013**, *3*, 2613.

(11) Capone, S.; Manera, M. G.; Taurino, A.; Siciliano, P.; Rella, R.; Luby, S.; Benkovicova, M.; Siffalovic, P.; Majkova, E. Fe_3O_4/γ-Fe_2O_3 Nanoparticle Multilayers Deposited by the Langmuir–Blodgett Technique for Gas Sensors Application. *Langmuir* **2014**, *30*, 1190–1197.

(12) Fainberg, A. Explosives Detection for Aviation Security. *Science* **1992**, *255*, 1531–1537.

(13) Baia, M.; Toderas, F.; Baia, L.; Popp, J.; Astilean, S. Probing the Enhancement Mechanisms of SERS with p-Aminothiophenol Molecules Adsorbed on Self-Assembled Gold Colloidal Nanoparticles. *Chem. Phys. Lett.* **2006**, *422*, 127–132.

(14) Carles, R.; Farcau, C.; Bonafos, C.; Benassayag, G.; Bayle, M.; Benzo, P.; Groenen, J.; Zwick, A. Three Dimensional Design of Silver Nanoparticle Assemblies Embedded in Dielectrics for Raman Spectroscopy Enhancement and Dark-Field Imaging. *ACS Nano* **2011**, *5*, 8774–8782.

(15) Li, X. L.; Zhang, J. H.; Xu, W. Q.; Jia, H. Y.; Wang, X.; Yang, B.; Zhao, B.; Li, B. F.; Ozaki, Y. Mercaptoacetic Acid-Capped Silver Nanoparticles Colloid: Formation, Morphology, and SERS Activity. *Langmuir* **2003**, *19*, 4285–4290.

(16) Park, J.; Gomez, A. L.; Walser, M. L.; Lin, A.; Nizkorodov, S. A. Ozonolysis and Photolysis of Alkene-Terminated Self-Assembled Monolayers on Quartz Nanoparticles: Implications for Photochemical Aging of Organic Aerosol Particles. *Phys. Chem. Chem. Phys.* **2006**, *8*, 2506–2512.

(17) Han, Y.; Lupitskyy, R.; Chou, T.-M.; Stafford, C. M.; Du, H.; Sukhishvili, S. Effect of Oxidation on Surface-Enhanced Raman Scattering Activity of Silver Nanoparticles: A Quantitative Correlation. *Anal. Chem.* **2011**, *83*, 5873–5880.

(18) Siffalovic, P.; Chitu, L.; Majkova, E.; Vegso, K.; Jergel, M.; Luby, S.; Capek, I.; Satka, A.; Maier, G. A.; Keckes, J.; Timmann, A.; Roth, S. V. Kinetics of Nanoparticle Reassembly Mediated by UV-Photolysis of Surfactant. *Langmuir* **2010**, *26*, 5451–5455.

(19) Renaud, G.; Lazzari, R.; Leroy, F. Probing Surface and Interface Morphology with Grazing Incidence Small Angle X-Ray Scattering. *Surf. Sci. Rep.* **2009**, *64*, 255–380.

(20) Renaud, G.; Lazzari, R.; Revenant, C.; Barbier, A.; Noblet, M.; Ulrich, O.; Leroy, F.; Jupille, J.; Borensztein, Y.; Henry, C. R.; et al. Real-Time Monitoring of Growing Nanoparticles. *Science* **2003**, *300*, 1416–1419.

(21) Müller-Buschbaum, P. A. Basic Introduction to Grazing Incidence Small-Angle X-Ray Scattering. In *Applications of Synchrotron Light to Scattering and Diffraction in Materials and Life Sciences*; Gomez, M., Nogales, A., Garcia-Gutierrez, M. C., Ezquerra, T. A., Eds.; Springer: Berlin/Heidelberg, Germany, 2009.

(22) Chitu, L.; Siffalovic, P.; Majkova, E.; Jergel, M.; Vegso, K.; Luby, S.; Capek, I.; Satka, A.; Perlich, J.; Timmann, A.; et al. Modified Langmuir-Blodgett Deposition of Nanoparticles - Measurement of 2D to 3D Ordered Arrays. *Meas. Sci. Rev.* **2010**, *10*, 162–165.

(23) Vegso, K.; Siffalovic, P.; Weis, M.; Jergel, M.; Benkovicova, M.; Majkova, E.; Chitu, L.; Halahovets, Y.; Luby, S.; Capek, I.; et al. In Situ GISAXS Monitoring of Langmuir Nanoparticle Multilayer Degradation Processes Induced by UV Photolysis. *Phys. Status Solidi A* **2011**, *208*, 2629–2634.

(24) Vegso, K.; Siffalovic, P.; Majkova, E.; Jergel, M.; Benkovicova, M.; Kocsis, T.; Weis, M.; Luby, S.; Nygard, K.; Konovalov, O. Nonequilibrium Phases of Nanoparticle Langmuir Films. *Langmuir* **2012**, *28*, 10409–10414.

(25) Jeng, U.-S.; Su, C. H.; Su, C.-J.; Liao, K.-F.; Chuang, W.-T.; Lai, Y.-H.; Chang, J.-W.; Chen, Y.-J.; Huang, Y.-S.; Lee, M.-T.; et al. A Small/Wide-Angle X-ray Scattering Instrument for Structural Charac-

terization of Air-Liquid Interfaces, Thin Films and Bulk Specimens. *J. Appl. Crystallogr.* **2010**, *43*, 110–121.
(26) Vegso, K.; Siffalovic, P.; Benkovicova, M.; Jergel, M.; Luby, S.; Majkova, E.; Capek, I.; Kocsis, T.; Perlich, J.; Roth, S. V. GISAXS Analysis of 3D Nanoparticle Assemblies—Effect of Vertical Nanoparticle Ordering. *Nanotechnology* **2012**, *23*, 045704.
(27) Heitsch, A. T.; Patel, R. N.; Goodfellow, B. W.; Smilgies, D. M.; Korgel, B. A. GISAXS Characterization of Order in Hexagonal Monolayers of FePt Nanocrystals. *J. Phys. Chem. C* **2010**, *114*, 14427–14432.
(28) Als-Nielsen, J.; MacMorrow, D. *Elements of Modern X-ray Physics*; Wiley: Chichester, UK, 2011.
(29) PDF-2 database of the International Center for Diffraction Data: Silver – file no. 00–004–0783; silver oxide – file no. 00–043–1038.
(30) Vegso, K.; Siffalovic, P.; Jergel, M.; Weis, M.; Benkovicova, M.; Majkova, E.; Luby, S.; Kocsis, T.; Capek, I. Silver Nanoparticle Monolayer-to-Bilayer Transition at the Air/Water Interface as Studied by the GISAXS Technique: Application of a New Paracrystal Model. *Langmuir* **2012**, *28*, 9395–9404.